Interface engineering of porous nickel-iron phosphates with enriched oxygen vacancies as an efficient bifunctional electrocatalyst for high current water splitting

Lixia Wang [a], Hongbo Yu [a], Zhiyang Huang [a], Zuyang Luo [a], Tayirjan Taylor Isimja [c,*], Shoulei Xu [b,*], Xiulin Yang [a,*]

[a] *Guangxi Key Laboratory of Low Carbon Energy Materials, School of Chemistry and Pharmaceutical Sciences, Guangxi Normal University, Guilin 541004, China*
[b] *School of Physical Science and Technology, Guangxi University, 100 East Daxue Road, Nanning 530004, China*
[c] *Saudi Arabia Basic Industries Corporation (SABIC), King Abdullah University of Science and Technology (KAUST), Thuwal 23955-6900, Saudi Arabia*

ARTICLE INFO

ABSTRACT

The delicate design of non-precious metal-based bifunctional electrocatalysts for simultaneous oxygen/hydrogen evolution reactions is pivotal for developing green and sustainable energy sources. Here, we have fabricated a novel nickel-iron phosphate heterostructure with abundant oxygen vacancies ($Fe_{0.86}Ni_{0.14}$-PO_x/CC) *via* hydrothermal reaction and gas-phase phosphating treatment. By appropriately adjusting the ratio of Ni/Fe, the electronic structure is regulated, thereby optimizing the oxygen vacancies to form abounded electrocatalytic active centers on the catalyst surface. The obtained $Fe_{0.86}Ni_{0.14}$-PO_x/CC catalyst reveals low overpotentials of 247 and 125 mV for OER and HER at a current density of 10 mA cm^{-2}, respectively. Besides, the overall water splitting electrolyzer originated from $Fe_{0.86}Ni_{0.14}$-PO_x/CC only requires a cell voltage of 2.01 V to deliver a current density of 500 mA cm^{-2} with good stability of 100 h (10 mA cm^{-2}). Importantly, $Fe_{0.86}Ni_{0.14}$-PO_x/CC possess 96.9 and 97.7% Faradaic yield for the generation of H_2 and O_2, respectively. This work invokes new feasibility for developing robust and cost-effective phosphate catalysts for electrochemical overall water splitting.

1. Introduction

High energy density and zero pollutant emission Hydrogen (H_2) generation through electrochemical overall water splitting (OWS) has been identified as the most attractive strategy to solve the energy crisis and environmental pollution [1,2]. During the OWS process, hydrogen evolution reaction (HER) occurs at the cathode and oxygen evolution reaction (OER) at the anode spontaneously [3]. Nevertheless, OWS remains an enormous challenge due to intrinsically sluggish kinetics and high overpotentials [4]. More importantly, the current density required by a practical industrial alkaline electrolyzer is usually between 200 and 500 mA cm^{-2} or even up to 1000 mA cm^{-2} [5,6]. Currently, Pt/C and IrO_2/RuO_2 are the most inherently active noble metal catalysts [7]. However, prohibitive cost, scarce resource and lack of long-term stability have dramatically plagued their widespread application [8,9]. In contrast, transition metal-based compounds are promising alternatives to noble metal-based catalysts due to their abundance, cost-effectiveness and durability [10,11]. Generally, the catalyst performance largely

depends on accessible active sites and conductivity [12]. Consequently, there are three promising strategies to enhance the performance of HER and OER simultaneously: (i) Rational design of catalyst morphology and structure to expose more active sites, thus accelerating reaction rates [13,14]. (ii) Tuning the catalyst's electronic structure to generate oxygen vacancies [15]. (iii) Creating synergistic interactions between different components can facilitate electron transfer, significantly reducing the reaction energy barrier [16,17].

Transition metal phosphates exhibit unusual catalytic activity due to their unique chemical properties and tunable versatility [18,19]. The phosphate groups can not only act as a proton acceptor promoting the oxidation of metal atoms but can also induce locally distorted metal geometry favouring water adsorption and oxidation [20]. Furthermore, transition metal oxides featuring iron and nickel elements showed a promising bifunctional nature due to their intrinsic catalytic activity [19]. Most importantly, the iron/nickel oxide composites containing surface oxygen vacancies are crucial for enhancing the catalyst performance. On the one hand, the oxygen vacancies create an excess local

---

electron and coordinative unsaturation that provide specific sites to bind small molecules. On the other hand, they are inherent defects of catalysts without introducing any foreign elements, which are beneficial to maintain structural integrity and durability [21]. Additionally, the rational design of self-supporting catalysts improves the mechanical robustness of electrodes [17]. Therefore, a composite carefully constructed by $Ni(PO_3)_2$ with oxygen vacancy-rich $FePO_4$ on carbon cloth is expected to be an ideal bifunctional electrocatalyst.

Encouraged by the above considerations, a novel oxygen-vacancy-rich $Fe_{0.86}Ni_{0.14}-PO_x$ nanosheet heterostructure was grown *in situ* on carbon cloth (CC) using a facile one-step hydrothermal and phosphating. The local electronic structure was tuned to enhance electrocatalytic activity by integrating the heterogeneous interfaces and oxygen vacancies into a single electrocatalyst. The $Fe_{0.86}Ni_{0.14}-PO_x$ demonstrates fine bifunctional catalytic activity and long-term stability. Meanwhile, the electrolyzer assembled employing $Fe_{0.86}Ni_{0.14}-PO_x$ achieved an ultra-low cell voltage of 2.01 V at 500 mA cm^{-2}, slightly better than the benchmark $RuO_2/CC^{(+)}||Pt-C/CC^{(-)}$ catalysts. Besides, $Fe_{0.86}Ni_{0.14}-PO_x/CC^{(+)}||Fe_{0.86}Ni_{0.14}-PO_x/CC^{(-)}$ revealed good durability over 100 h at 10 mA cm^{-2} under alkaline conditions.

2. Experimental

2.1. Materials

Nickel nitrate hexahydrate ($Ni(NO_3)_2\cdot6H_2O$, ≥98%), Iron nitrate nonahydrate ($Fe(NO_3)_3\bullet9H_2O$), ethanol absolute (C_2H_5OH, ≥99.7%), Nafion (5% solution), sodium hypophosphite monohydrate ($NaH_2PO_2\cdot H_2O$, 99%), and potassium hydroxide (KOH) were purchased from Guangxi Zoey Biotechnology Co., Ltd. Urea ($CO(NH_2)_2$) and ammonium fluoride (NH_4F) was acquired from Xilong Science Co., Ltd. All reagents are analytical grade and were used without further purification. Commercial Pt/C (20 wt% for platinum) was purchased from Alfa Aesar. The carbon cloth (CC) substrate used in the experiments with a dimension of 3 cm × 1.5 cm.

2.2. Synthesis of Fe_xNi_y-LDH on carbon cloth

The CC was ultrasonically washed with 0.5 M H_2SO_4, deionized water and ethanol for 15 min to remove impurities. $FeOOH-Ni(OH)_2$ was grown on CC by a one-step hydrothermal method. In detail, 4.1 mmol $Fe(NO_3)_3\cdot9H_2O$, 0.7 mmol $Ni(NO_3)_2\cdot6H_2O$, 3.2 mmol NH_4F, and 8.0 mmol urea were dissolved in 60 mL deionized water, and 5 mL ethanol stirred at room temperature for 30 min to obtain a clear solution. Then the obtained solution was transferred to a Teflon-lined autoclave (100 mL) with a piece of treated CC, and the hydrothermal reaction was performed at 120 °C for 12 h. After natural cooling to room temperature, the modified CC material was washed several times with deionized water and then dried in an oven at 60 °C for 2 h. The obtained composites were named as Fe_xNi_y-LDH/CC according to the Fe/Ni ratio (x/y). A series of composites with different Fe/Ni ratios were synthesized, the total amount of Fe^{3+} and Ni^{2+} was 4.8 mmol, and the molar ratios of Fe/Ni were 1/0, 1/4, 1/6, 1/8 and 0/1, respectively.

2.3. Synthesis of Fe_xNi_y-PO_x/CC by vapor phase phosphidation

A piece of $Fe_{0.86}Ni_{0.14}$-LDH and 1.0 g of $NaH_2PO_2\cdot H_2O$ were placed downstream and upstream of a tube furnace, respectively. Afterwards, the tube furnace was heated to 300 °C in a N_2 atmosphere (20 sccm) at a heating rate of 5 min^{-1} for 2 h. Then, the resultant products were rinsed with deionized water and dried in an oven at 60 °C for 2 h. The prepared sample was named as $Fe_{0.86}Ni_{0.14}-PO_x/CC$. Subsequently, a series of samples were prepared using a similar method described above and called $Fe_{0.80}Ni_{0.20}-PO_x/CC$, $Fe_{0.89}Ni_{0.11}-PO_x/CC$, Fe-$PO_x/CC$ and Ni-PO_x/CC, respectively.

2.4. Synthesis of Pt-C/CC and RuO_2/CC

For comparison, we also prepared RuO_2 and commercial Pt/C modified on CC. 2 mg RuO_2 or commercial Pt/C was dispersed in 400 μL of deionized water/ethanol (V/V = 1:1) and 5 μL 5% Nafion as a binder to form a homogeneous catalyst ink. Then, the mixture was drop-casted onto the CC surface (1 cm × 1 cm) and dried in the air.

3. Results and discussion

3.1. Structural and morphological characterizations

The synthesis process of $Fe_{0.86}Ni_{0.14}-PO_x/CC$ is presented in Fig. 1a. Firstly, nanosheet-like Fe_xNi_y-LDH was grown vertically on the CC surface at 120 °C for 12 h. Subsequently, the $Fe_xNi_y-PO_x/CC$ was obtained by pyrolysis at 300 °C for 2 h under a N_2 atmosphere with NaH_2PO_2 as a P source. The X-ray diffraction (XRD) patterns confirm the precursor's composition and heterostructure catalysts. Fig. S2a shows the XRD pattern of $Fe_{0.86}Ni_{0.14}$-LDH/CC precursor, in which the diffraction peak is well corroborated as the peak of FeOOH (JCPDS: 34–1266) and Ni (OH)$_2$ (JCPDS: 38–0715) [22,23]. Figs. S2b and 1b reveal the XRD patterns of $Fe_{0.86}Ni_{0.14}-PO_x/CC$ and samples with different Fe/Ni ratios index into the standard characteristic peaks of $FePO_4$ (JCPDS: 50–1635) and $Ni(PO_3)_2$ (JCPDS: 28–0708) [24,25], indicating the $Ni(PO_3)_2/FePO_4$ heterojunction structure was successfully synthesized. Brunauer-Emmett-Teller (BET) gas adsorption tests were carried out on catalysts with different Fe/Ni ratios (Figs. 1c and S3). The N_2 adsorption-desorption isotherm curve of $Fe_{0.86}Ni_{0.14}-PO_x/CC$ illustrates that the BET surface area is 54.8 $m^2\ g^{-1}$, a typical IV-type isothermal process [26]. In addition, the average BJH pore diameters of $Fe_{0.86}Ni_{0.14}-PO_x/CC$ is 34.8 nm are significantly higher than those of $Fe_{0.80}Ni_{0.20}-PO_x/CC$ (23.0 nm), $Fe_{0.89}Ni_{0.11}-PO_x/CC$ (19.5 nm), Fe-PO_x/CC (21.9 nm), and Ni-PO_x/CC (19.2 nm). The high porosity of $Fe_{0.86}Ni_{0.14}-PO_x/CC$ facilitates the mass transfer and exposes plenty of accessible active sites, thereby, greatly enhancing the electrocatalytic performance [27,28]. The electron paramagnetic resonance (EPR) spectra (Fig. 1d) exhibited that the obtained catalysts, except for Ni-PO_x, show an intense resonance signal ($g \approx 2.0$) and the signal is enhanced with the increase of Fe ratio, suggesting that the presence of Fe favors the formation of oxygen vacancies [29]. Our results show that a high concentration of oxygen vacancies have been successfully created in $Fe_xNi_y-PO_x/CC$ and can be controlled by adjusting the Fe content. This is beneficial for increasing the rate of the electrocatalytic reaction and enhancing catalytic activity. Similar findings also reported in the literature [30]. Previous studies have elucidated that the introduction of vacancies in the catalyst can significantly provide additional active sites while further activating the residual inert substrates on its surface, thereby increasing the activity of individual sites and favorably reducing the overpotential of the reaction [31,32].

The morphology and microstructure of the catalysts were characterized using scanning electron microscopy (SEM). The surface of the pristine CC was initially smooth (Fig. S4) and turned into a well-aligned nanosheets-like structure after *in situ* hydrothermal growth of $Fe_{0.86}Ni_{0.14}$-LDH as illustrated in Fig. 2a. After the calcination of $Fe_{0.86}Ni_{0.14}$-LDH precursor at 300 °C, the morphology of $Fe_{0.86}Ni_{0.14}-PO_x/CC$ is similar with that of $Fe_{0.86}Ni_{0.14}$-LDH/CC. At the same time, the nanosheets became larger and thinner during the phosphorylation process (Fig. 2b). Transmission electron morphology (TEM) image (Fig. 2c) further confirms that the resulting $Fe_{0.86}Ni_{0.14}-PO_x/CC$ is layered nanosheet morphology, providing abundant active sites for the electrocatalytic reaction [11]. The high-resolution TEM (HR-TEM) image displays the distinct interplanar spacing of 0.265 and 0.356 nm, which are associated with the (400) and (−323) planes of $Ni(PO_3)_2$, respectively. In comparison, lattice fringes of 0.268 and 0.253 nm are attributed to the (103) and (110) planes of $FePO_4$ (Fig. 2d). The above results further demonstrate the successful fabrication of $Ni(PO_3)_2/FePO_4$

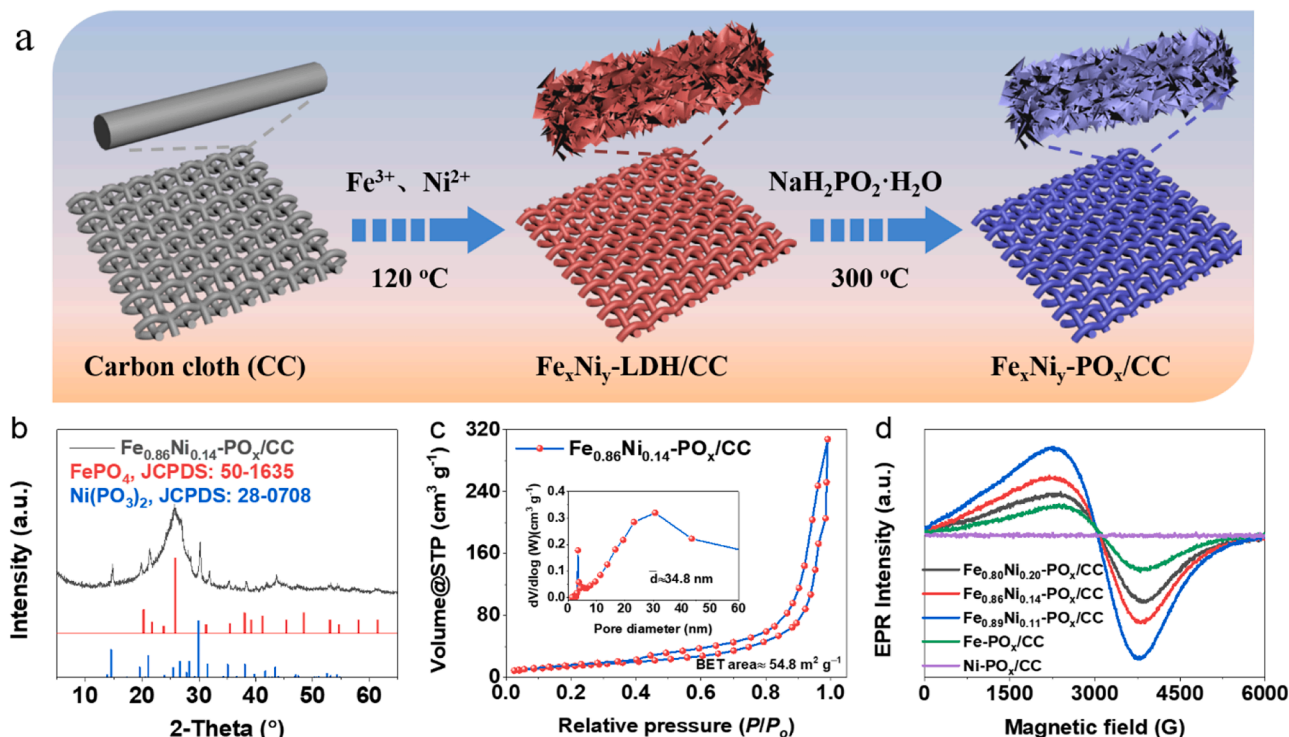**Fig. 1.** (a) Schematic illustration of the fabrication of Fe_xNi_y-PO_x/CC electrocatalysts. (b) XRD pattern, and (c) Nitrogen adsorption-desorption isotherm of $Fe_{0.86}Ni_{0.14}$-PO_x/CC. (d) EPR spectra of Fe_xNi_y-PO_x samples with different Fe/Ni ratios.

heterojunction. Moreover, from the selective area electron diffraction (SAED) pattern (Fig. 2e), the diffraction rings matched well with the (-323) plane of $Ni(PO_3)_2$ and the $(110)/(204)$ planes of $FePO_4$. Meanwhile, Energy-dispersive X-ray spectroscopy (EDS) in Fig. 2f, the high-angle circular dark-field scanning TEM (HAADF-STEM) image and corresponding elemental mappings (Fig. 2g) verify that Ni, Fe, P and O elements are uniformly distributed throughout the $Fe_{0.86}Ni_{0.14}$-PO_x/CC nanosheets. Correspondingly, the ICP-MS results showed accurate elemental contents, in which the fractions of Fe and Ni were 21.08 and 1.56 wt%, respectively (Table S1).

X-ray photoelectron spectroscopy (XPS) was performed to detect the surface chemical composition and valence state of $Fe_{0.86}Ni_{0.14}$-PO_x/CC. As depicted in Fig. 3a, the full survey spectrum of $Fe_{0.86}Ni_{0.14}$-PO_x/CC indicates the presence of Fe, Ni, P and O elements, which is consistent with the XRD and TEM results. The high-resolution C 1s spectrum is deconvoluted into four peaks, and including C=C (284.0 eV), C–C (284.8 eV), C–O (286.0 eV) and C=O (288.6 eV) in Fig. 3b [33]. Simultaneously, the binding energies are calibrated with C 1s as the standard [34]. As displayed in Fig. 3c, the high-resolution XPS spectrum of Fe 2p in $Fe_{0.86}Ni_{0.14}$-PO_x/CC shows Fe $2p_{3/2}$ at 706.6 eV, 710.2 eV, 713.0 eV and 716.9 can be deconvoled into Fe-P, Fe^{2+}, Fe^{3+} and satellite peak [35,36]. The Ni 2p spectrum (Fig. 3d) presents three pairs of peaks corresponding to the Ni−P bond (853.0/870.1 eV), Ni−O bond (856.1/837.8 eV), and satellite peaks (861.1/879.8 eV) [37,38]. As summarized in Fig. 3e, the O 1 s spectrum of $Fe_{0.86}Ni_{0.14}$-PO_x/CC indicates four main peaks located at 530.0, 530.8, and 532.2 eV, which are assigned to M-O, oxygen vacancies and H_2O_{ads}, respectively [39,40]. The P 2p core energy level spectrum of $Fe_{0.86}Ni_{0.14}$-PO_x/CC is shown in Fig. 3f, the peak at 133.2 eV is attributed to the P-O bond, and the two fitted peaks at 128.7 and 129.7 eV are assigned to the P $2p_{3/2}$ and P $2p_{1/2}$, respectively [41]. As expected, XPS analysis substantiated the successful preparation of $Ni(PO_3)_2$ and $FePO_4$.

3.2. Electrocatalytic performance

The electrocatalytic OER activities of $Fe_{0.86}Ni_{0.14}$-PO_x/CC and corresponding control samples were studied in 1.0 M KOH using a standard three-electrode setup. Fig. 4a shows the OER polarization curves for all samples. There is a significant increase in the OER activity of Fe_xNi_y-PO_x/CC compared to single Ni-PO_x/CC and Fe-PO_x/CC electrodes, suggesting that interface engineering is beneficial to achieve better performance. Specifically, the overpotentials of $Fe_{0.86}Ni_{0.14}$-PO_x/CC, $Fe_{0.89}Ni_{0.11}$-PO_x/CC, $Fe_{0.80}Ni_{0.20}$-PO_x/CC, Ni-PO_x/CC, Fe-PO_x/CC, and RuO_2/CC are 247, 272, 292, 377, 457 and 247 mV at a current density of 10 mA cm^{-2}, respectively. As expected, the $Fe_{0.86}Ni_{0.14}$-PO_x/CC possesses a good OER performance with a low Tafel slope of 48.3 mV dec^{-1}. It is substantially lower than the $Fe_{0.89}Ni_{0.11}$-PO_x/CC (69.5 mV dec^{-1}), $Fe_{0.80}Ni_{0.20}$-PO_x/CC (73.0 mV dec^{-1}), Ni-PO_x/CC (117.5 mV dec^{-1}), Fe-PO_x/CC (74.5 mV dec^{-1}), and RuO_2/CC (59.9 mV dec^{-1}), implying the fast OER reaction kinetics of $Fe_{0.86}Ni_{0.14}$-PO_x/CC (Fig. 4b) [42]. The OER performance of $Fe_{0.86}Ni_{0.14}$-PO_x/CC also exceeds those of most recently reported OER electrocatalysts (Fig. 4c and Table S2). Electrochemical impedance spectroscopy (EIS) can reflect the interfacial charge transfer rate of the catalyst [2]. As illustrated in Fig. 4d, the charge transfer resistance (R_{ct}) of Fe_xNi_y-PO_x/CC is lower than that of Ni-PO_x/CC and Fe-PO_x/CC, indicating the heterointerfaces between Ni $(PO_3)_2$ and $FePO_4$ can improve the electrical conductivity and charge transfer of the catalyst. Among them, $Fe_{0.86}Ni_{0.14}$-PO_x/CC has the lowest R_{ct}, which is beneficial to charge transfer during the OER process and can accelerate the reaction progress [41]. Double-layer capacitance (C_{dl}) was also executed to investigate the influence of the electrochemically active surface area (ECSA) on electrochemical properties. The ECSA is derived from the C_{dl} of the cyclic voltammetry (CV) curve in the non-Faradaic range (Fig. S5). The fitted C_{dl} is displayed in Fig. 4e. Appreciably, the C_{dl} value of $Fe_{0.86}Ni_{0.14}$-PO_x/CC is 99.7 mF cm^{-2}, which is higher than those of $Fe_{0.89}Ni_{0.11}$-PO_x/CC (14.0 mF cm^{-2}), $Fe_{0.80}Ni_{0.20}$-PO_x/CC (34.7 mF cm^{-2}), Ni-PO_x/CC (2.1 mF cm^{-2}), and Fe-PO_x/CC (5.6 mF cm^{-2}), respectively. The above results are consistent

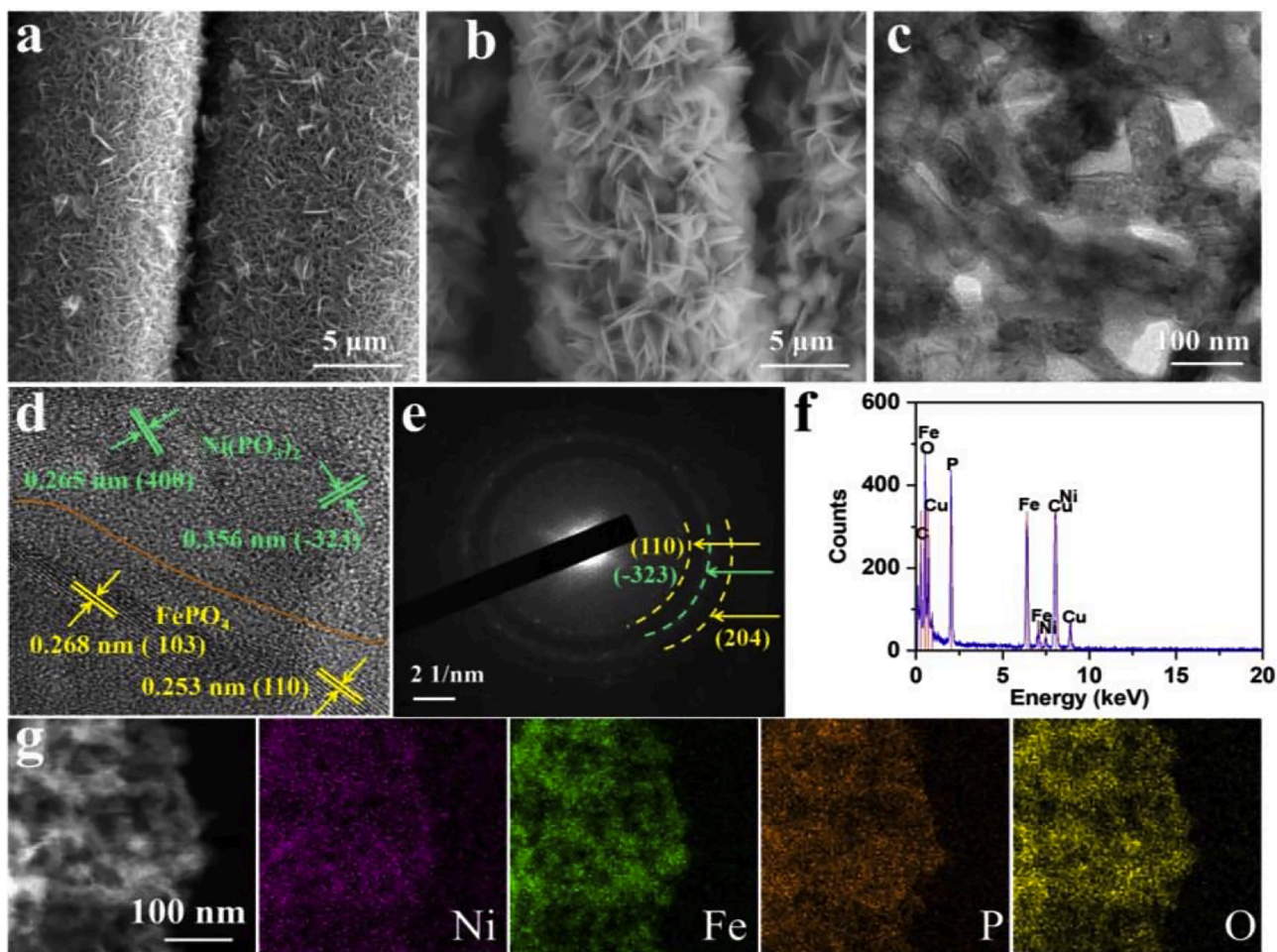**Fig. 2.** (a) SEM image of FexNiy-LDH/CC. (b) SEM image, (c) TEM image, (d) high-resolution TEM image, (e) SAED image, (f) EDS pattern, and (g) HAADF-STEM image and corresponding element mappings of $Fe_{0.86}Ni_{0.14}$-PO_x/CC.
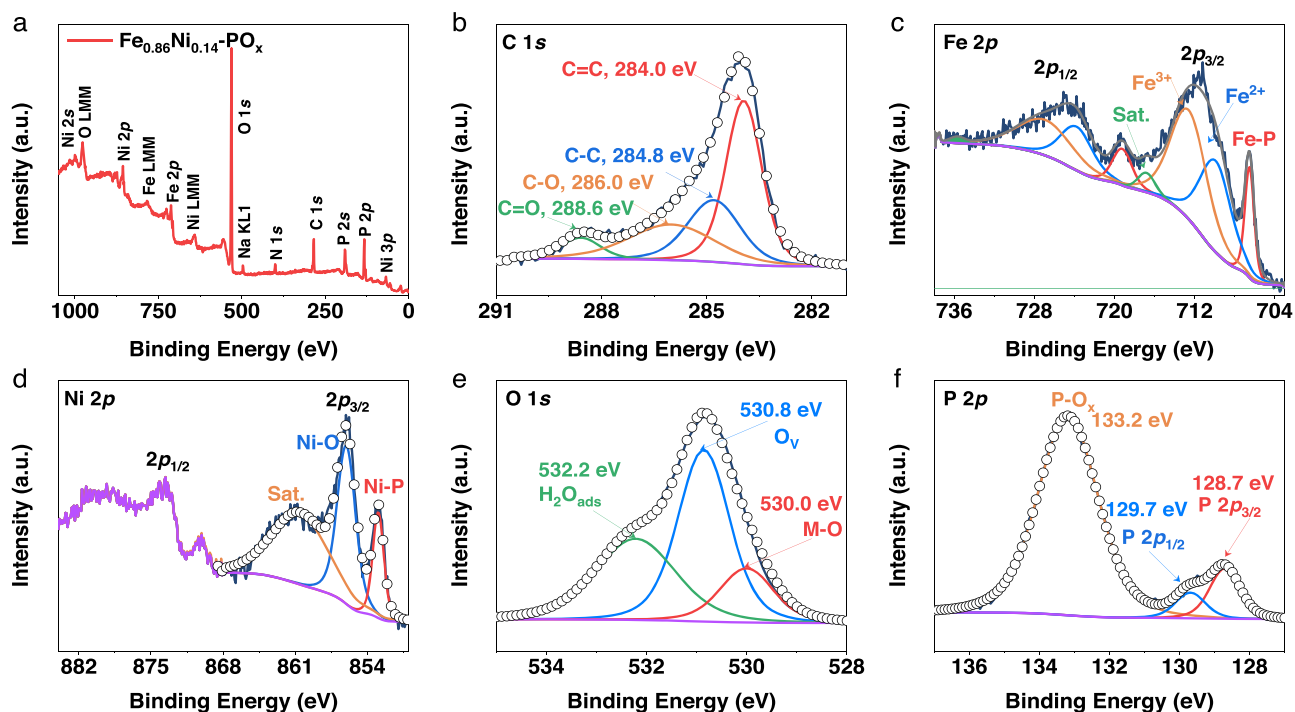

Fig. 3. (a) Full-range XPS survey of $Fe_{0.86}Ni_{0.14}$-PO_x/CC. High-resolution XPS spectra of (b) C 1s, (c) Fe 2p, (d) Ni 2p, (e) O 1s, and (f) P 2p of $Fe_{0.86}Ni_{0.14}$-PO_x/CC.

Fig. 4. OER performance of different electrocatalysts in 1.0 M KOH solution. (a) LSV polarization curves, and (b) corresponding tafel slopes. (c) Comparison with the overpotentials and tafel slopes of recently reported catalysts for OER activity at 10 mA cm^{-2}. (d) Electrochemical impedance spectroscopy (EIS), and (e) double layer capacitance (C_{dl}) of different electrocatalysts. (f) Chronopotentiometry curve of $Fe_{0.86}Ni_{0.14}$-PO$_x$/CC at a constant current density of 10 mA cm^{-2} for 100 h.

with ECSA, as shown in Fig. S6. The ECSA value of $Fe_{0.86}Ni_{0.14}$-PO$_x$/CC is 1661.7 cm^2, which is significantly larger than those of $Fe_{0.89}Ni_{0.11}$-PO$_x$/CC (233.3 cm^2), $Fe_{0.80}Ni_{0.20}$-PO$_x$/CC (578.3 cm^2), Ni-PO$_x$/CC (35.0 cm^2) and Fe-PO$_x$/CC (93.3 cm^2), further demonstrating that the interfacial synergy between Ni-PO$_x$/CC and Fe-PO$_x$/CC enhances the intrinsic activity of $Fe_{0.86}Ni_{0.14}$-PO$_x$/CC heterostructure catalyst [43]. Larger ECSA is beneficial for exposing more available active sites,

accelerating mass transfer and promoting electrocatalytic activity [44]. Remarkably, long-term stability is an important parameter affecting the catalyst's prevalent application. The chronopotentiometry was conducted at a current density of 10 mA cm^{-2} for 100 h to assess the OER durability of $Fe_{0.86}Ni_{0.14}$-PO$_x$/CC in 1.0 M KOH solution (Fig. 4f). It exhibited negligibly potential changes, which implement that $Fe_{0.86}Ni_{0.14}$-PO$_x$/CC possesses robust stability.
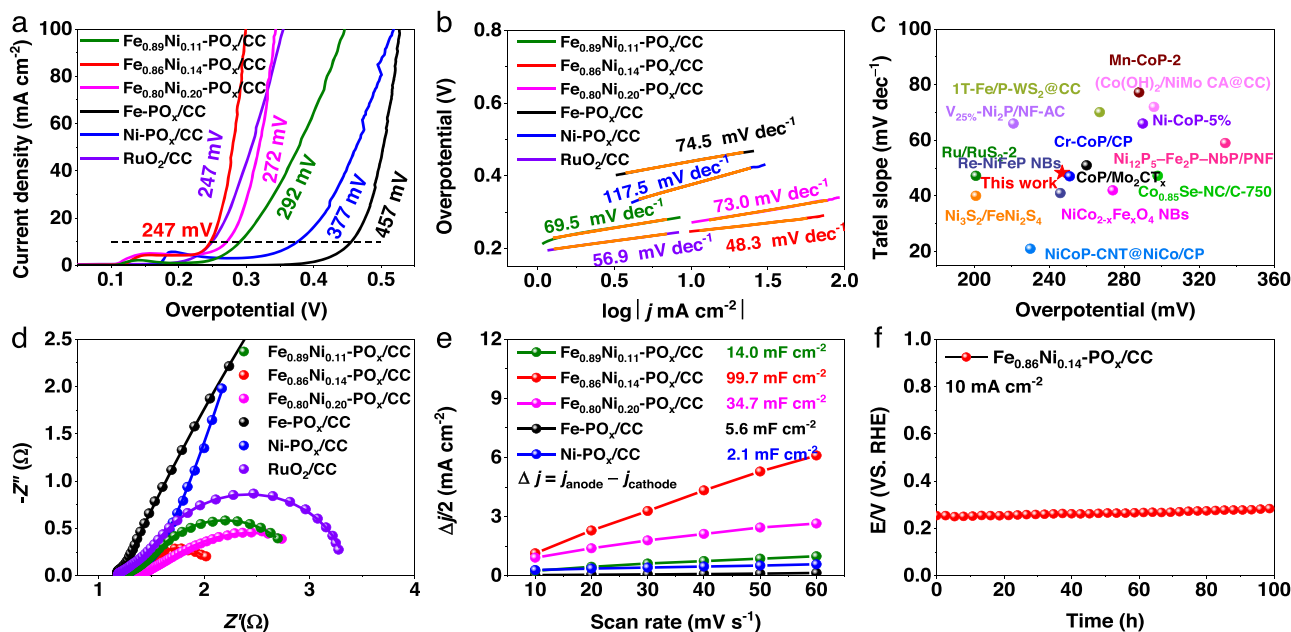
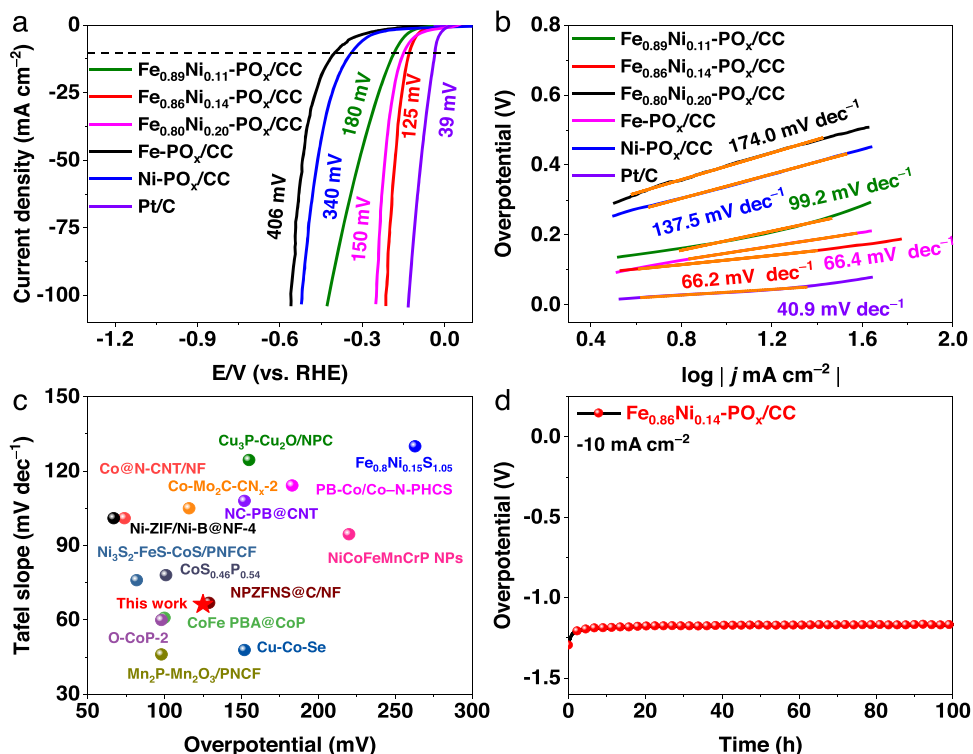

Fig. 5. HER performance of different electrocatalysts in 1.0 M KOH solution. (a) LSV polarization curves, and (b) corresponding tafel slopes. (c) Comparison with the overpotentials and tafel slopes of recently reported catalysts for HER activity at −10 mA cm^{-2}. (d) Chronopotentiometry curve of $Fe_{0.86}Ni_{0.14}$-PO$_x$/CC at a constant current density of −10 mA cm^{-2} for 100 h.

Following the HER performance of $Fe_{0.86}Ni_{0.14}$-PO_x/CC and other as-prepared samples are shown in Fig. 5a. The LSV curves demonstrate that the $Fe_{0.86}Ni_{0.14}$-PO_x/CC exhibits the highest HER activity among the as-prepared catalysts with the lowest overpotential of 125 mV at 10 mA cm^{-2}, which is significantly lower than that of $Fe_{0.89}Ni_{0.11}$-PO_x/CC (180 mV), $Fe_{0.80}Ni_{0.20}$-PO_x/CC (150 mV), Ni-PO_x/CC (340 mV) and Fe-PO_x/CC (406 mV), except for Pt/C (39 mV). As indicated in Fig. 5b, the Tafel slope of $Fe_{0.86}Ni_{0.14}$-PO_x/CC (66.2 mV dec^{-1}) is close to that of Pt/C (40.9 mV dec^{-1}) and lower than that of $Fe_{0.89}Ni_{0.11}$-PO_x/CC (99.2 mV dec^{-1}), $Fe_{0.80}Ni_{0.20}$-PO_x/CC (174.0 mV dec^{-1}), Ni-PO_x/CC (137.5 mV dec^{-1}) and Fe-PO_x/CC (66.4 mV dec^{-1}), manifesting that $Fe_{0.86}Ni_{0.14}$-PO_x/CC follows the Volmer-Heyrovsky HER mechanism [45]. In addition, the overpotential (at 10 mA cm^{-2}) and Tafel slope values of $Fe_{0.86}Ni_{0.14}$-PO_x/CC are also competitive compared with the recently reported HER catalysts (Fig. 5c and Table S3). Similarly, $Fe_{0.86}Ni_{0.14}$-PO_x/CC showed 100 h at -10 mA cm^{-2} stability without much voltage deviation, indicating its robust durability (Fig. 5d).

The highlighted bifunctional catalytic activity of $Fe_{0.86}Ni_{0.14}$-PO_x/CC relative to its comparison samples is encouraging. Consequently, a two-electrode electrolyzer ($Fe_{0.86}Ni_{0.14}$-PO_x/$CC^{(+)}$||$Fe_{0.86}Ni_{0.14}$-PO_x/$CC^{(-)}$) was further assembled using $Fe_{0.86}Ni_{0.14}$-PO_x/CC as anode and cathode catalysts for OWS in 1.0 M KOH. Fig. 6a displays a schematic diagram of two-electrode overall water splitting [46]. As expected, the $Fe_{0.86}Ni_{0.14}$-PO_x/$CC^{(+)}$||$Fe_{0.86}Ni_{0.14}$-PO_x/$CC^{(-)}$ demands only 2.01 V to achieve an industrial favored high current density of 500 mA cm^{-2} better than the RuO_2/$CC^{(+)}$||Pt-C/$CC^{(-)}$ in Fig. 6b. It is worth noting that the LSV curves of RuO_2/$CC^{(+)}$||Pt-C/$CC^{(-)}$ show significant fluctuation at current densities above 500 mA cm^{-2}. This is likely caused by the use of Nafion during the preparation of the electrode. Nafion may not provide adequate adhesion to withstand too many bubbles and may block active sites, hindering bubble diffusion and separation [17]. Meanwhile, this further illustrates the mechanical robustness of the $Fe_{0.86}Ni_{0.14}$-PO_x/CC electrode. In addition, its OWS performance in 1.0 M KOH exceeds those of many reported bifunctional catalysts (Fig. 6c and Table S4). Moreover, a stability test of the OWS was carried out to

confirm the practical application of the well-designed $Fe_{0.86}Ni_{0.14}$-PO_x/CC catalyst. As observed in Fig. 6d, it can be maintained at a current density of 10 mA cm^{-2} for 100 h with almost no noticeable degradation, verifying the notable stability and durability of $Fe_{0.86}Ni_{0.14}$-PO_x/CC in OWS.

3.3. Faradaic efficiency (FE) test

The amount of H_2 and O_2 generated by $Fe_{0.86}Ni_{0.14}$-PO_x/CC electrocatalyst was collected using the drainage method (Fig. 7a) [47]. The $Fe_{0.86}Ni_{0.14}$-PO_x/CC rapidly dissociated H_2O to create large amounts of H_2 and O_2 at a chronocurrent of 350 mA cm^{-2} in 1.0 M KOH (Fig. 7b,c) presents the volume change of O_2 while 10, 20, 30, 40 and 50 mL of H_2 were generated, respectively. As depicted in Fig. 7d, the FE of $Fe_{0.86}Ni_{0.14}$-PO_x/CC was calculated to be 96.9 and 97.7% for the generation of H_2 and O_2 respectively, and this slight loss may be caused by redox charges of the material [48], further validating the $Fe_{0.86}Ni_{0.14}$-PO_x/CC is an efficient bifunctional electrocatalyst.

3.4. Catalytic mechanism analysis

To explore the reaction mechanism of the electrocatalyst in the OER half-reaction, the $Fe_{0.86}Ni_{0.14}$-PO_x/CC was characterized by SEM and XPS after OER. The SEM image shows that the nanosheets on the $Fe_{0.86}Ni_{0.14}$-PO_x/CC surface became rough and slightly aggregated after stability testing (Fig. S7). As shown in Fig. S8, compared with the results before the OER test, Fe-P in Fe $2p$ spectrum became relatively weak, while the peak of Ni-P in Ni $2p$ disappeared utterly, indicating complete oxidation, which suggests that the role of metal-P is to generate unique catalyst morphology and porosity to expose more active sites. The high-resolution P $2p$ spectrum exhibits a peak of phosphorus oxide, whose intensity decreased significantly after the OER test, and the M-P bond-associated peaks nearly disappeared. Besides, the formation of Fe/Ni hydroxide or oxyhydroxide on the catalyst surface during the OER test [49] further confirms the critical role of phosphate. In addition, the
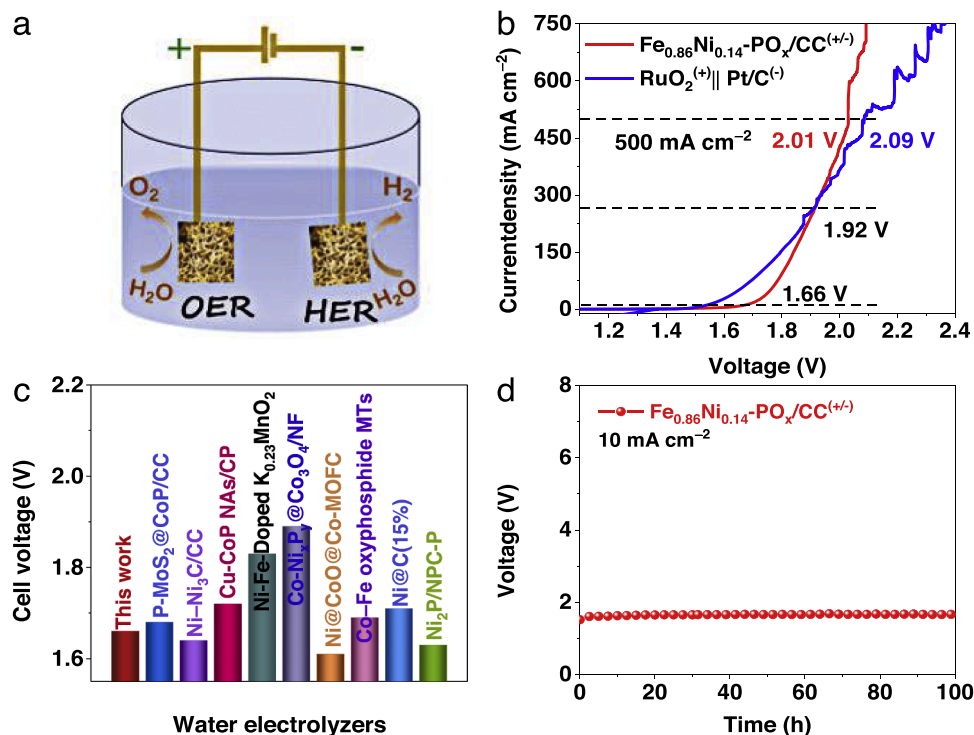
Fig. 6. (a) Schematic diagram of overall water splitting electrolyzer using $Fe_{0.86}Ni_{0.14}$-PO_x/CC as bifunctional catalyst. (b) Comparison of polarization curves of $Fe_{0.86}Ni_{0.14}$-PO_x/$CC^{(+)}$||$Fe_{0.86}Ni_{0.14}$-PO_x/$CC^{(-)}$ and the RuO_2/$CC^{(+)}$||Pt-C/$CC^{(-)}$ at high current density. (c) Comparing cell voltages with the recently reported electrolyzers at 10 mA cm^{-2}. (d) Long-term stability test of $Fe_{0.86}Ni_{0.14}$-PO_x/$CC^{(+)}$||$Fe_{0.86}Ni_{0.14}$-PO_x/$CC^{(-)}$ at 10 mA cm^{-2}.
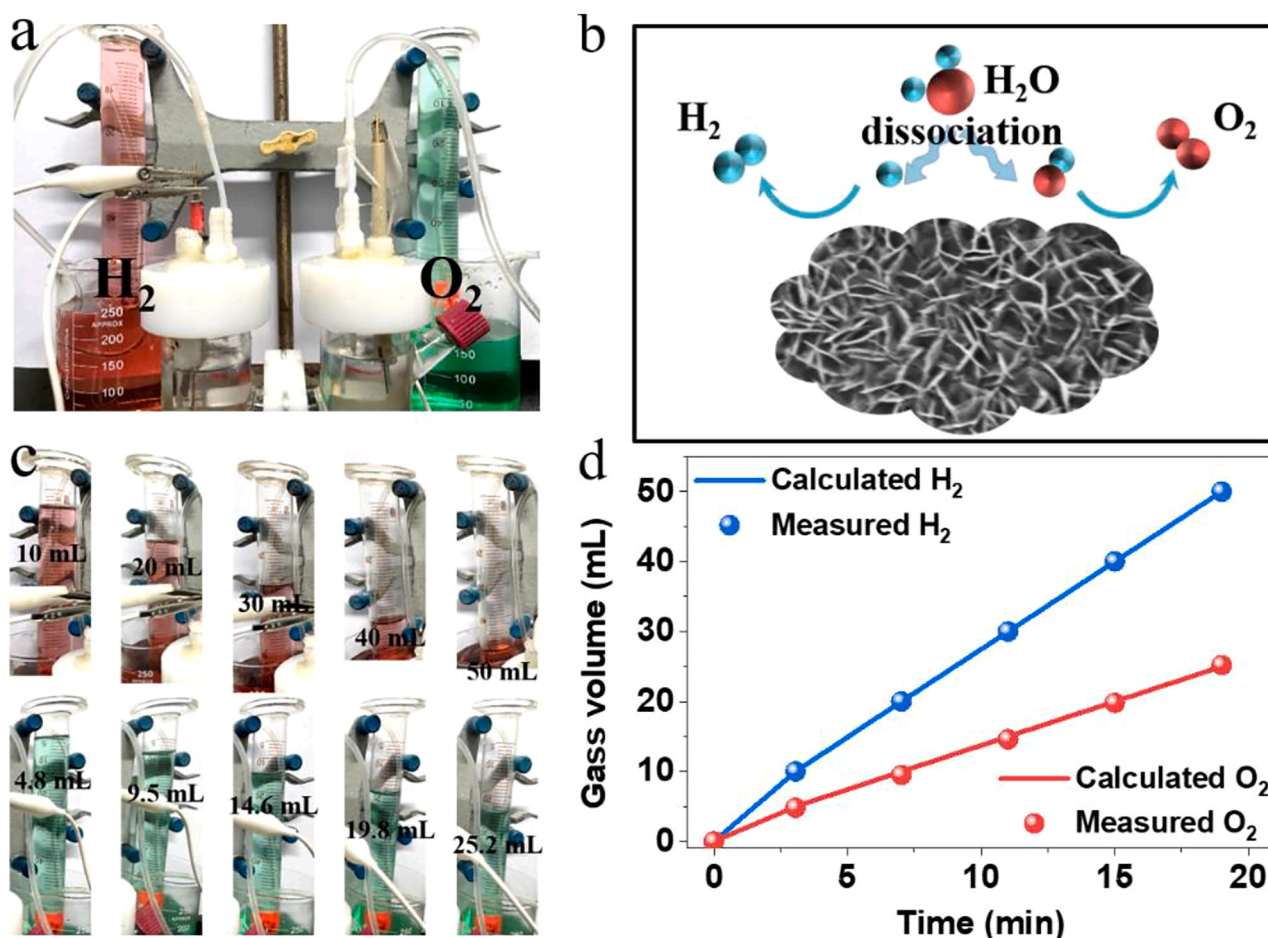
Fig. 7. (a) Gas collection device for H_2 and O_2 production of $Fe_{0.86}Ni_{0.14}-PO_x/CC$ electrocatalysts. (b) Schematic illustration of the prepared $Fe_{0.86}Ni_{0.14}-PO_x/CC$ for HER and OER. (c) Record the volume change of O_2 and the required reaction time to generate 10, 20, 30, 40 and 50 mL H_2, respectively. (d) The amount of gas theoretically calculated and experimentally measured for overall water splitting of $Fe_{0.86}Ni_{0.14}-PO_x/CC$.

high-resolution O 1s spectrum appeared at three peaks at 530.3, 531.2 and 532.2 eV, corresponding to the M-O, oxygen vacancies, and H_2O_{ads}, respectively. Notably, there is an enhanced O 1s peak of M-O, indicating that more O* was adsorbed on the surface of the catalyst during the alkaline OER process [50]. These results demonstrated that $Fe_{0.86}Ni_{0.14}-PO_x/CC$ was oxidized during the OER stability test.

Briefly, the satisfactory performance and stability of $Fe_{0.86}Ni_{0.14}-PO_x/CC$ in the alkaline electrolyte can be explained as follows: (i) The construction of nanosheet heterostructure provides a larger specific surface area, which accelerates the diffusion of active species and surface electron transfer. (ii) The interaction between different components of $Ni(PO_3)_2$ and $FePO_4$ interface is beneficial in adjusting the electronic structure to improve the catalytic activity. (iii) Oxygen vacancies engineering can effectively optimize the electronic structure of $Fe_{0.86}Ni_{0.14}-PO_x/CC$ to increase the intrinsic activity, thereby promoting the reaction kinetics.

4. Conclusion

In summary, we successfully fabricated $Fe_{0.86}Ni_{0.14}-PO_x/CC$ heterostructure nanosheet electrocatalyst with abundant oxygen vacancies. Due to the interfacial nanosheet structure with numerous oxygen vacancies, $Fe_{0.86}Ni_{0.14}-PO_x/CC$ exhibits good catalytic performance and robust stability for both OER and HER in alkaline electrolytes. Impressively, the obtained $Fe_{0.86}Ni_{0.14}-PO_x/CC$ showed a low overpotential of 247 mV to reach a current density of 10 mA cm^{-2} and high stability during OER, as well as good HER performance with an overpotential of

125 mV at 10 mA cm^{-2}. In addition, the overall water splitting device consisting of $Fe_{0.86}Ni_{0.14}-PO_x/CC$ can drive a current density of 500 mA cm^{-2} with only 2.01 V and maintain stability at 10 mA cm^{-2} for 100 h. The results highlight the importance of interfacial engineering and abundant oxygen vacancies for developing efficient and stable bifunctional electrocatalysts for water splitting that have tremendous potential for industrial applications.

CRediT authorship contribution statement

Lixia Wang: Conceptualization, Data curation, Writing – original draft. **Hongbo Yu:** Methodology, Data curation. **Zhiyang Huang:** Investigation. **Zuyang Luo:** Formal analysis. **Tayirjan Taylor Isimja:** Writing – review & editing. **Shoulei Xu:** Writing – review & editing. **Xiulin Yang:** Supervision, Writing – review & editing, Funding acquisition.

Declaration of Competing Interest

The authors declare that they have no known competing financial interests or personal relationships that could have appeared to influence the work reported in this paper.

Data availability

The authors do not have permission to share data.

Acknowledgments

This work has been supported by the National Natural Science Foundation of China (No. 21965005), Natural Science Foundation of Guangxi Province (2021GXNSFAA076001), Project of High-Level Talents of Guangxi (F-KA18015), and Guangxi Technology Base and Talent Subject (GUIKE AD18126001, GUIKE AD20297039).

Supplementary materials

Supplementary material associated with this article can be found, in the online version, at doi:10.1016/j.electacta.2023.141932.

References

[1] F.C. Pan, H. He, Z.X. Yang, Q. Zheng, D. Lin, Y. Huo, Rationally designed Ni_2P/ WS_2/Co_9S_8@C multi-interfacial electrocatalyst for efficient overall water splitting, Chem. Eng. J. 446 (2022), 136961.

[2] Y. Zhang, H. Liu, R. Ge, J. Yang, S. Li, Y. Liu, L. Feng, Y. Li, M. Zhu, W. Li, Mo-induced *in-situ* architecture of Ni_xCo_yP/Co_2P heterostructure nano-networks on nickel foam as bifunctional electrocatalysts for overall water splitting, Sustain. Mater. Technol. 33 (2022) e00461.

[3] W. Luo, Y. Wang, L. Luo, S. Gong, M. Wei, Y. Li, X. Gan, Y. Zhao, Z. Zhu, Z. Li, Single-atom and bimetallic nanoalloy supported on nanotubes as a bifunctional electrocatalyst for ultrahigh-current-density overall water splitting, ACS Catal. 12 (2022) 1167–1179.

[4] H. Ma, Z. Chen, Z. Wang, C.V. Singh, Q. Jiang, Interface engineering of Co/ CoMoN/NF heterostructures for high-performance electrochemical overall water splitting, Adv. Sci. 9 (2022), 2105313.

[5] Y. Luo, L. Tang, U. Khan, Q. Yu, H.M. Cheng, X. Zou, B. Liu, Morphology and surface chemistry engineering toward pH-universal catalysts for hydrogen evolution at high current density, Nat. Commun. 10 (2019) 269.

[6] C. Zhang, Y. Luo, J. Tan, Q. Yu, F. Yang, Z. Zhang, L. Yang, H.M. Cheng, B. Liu, High-throughput production of cheap mineral-based two-dimensional electrocatalysts for high-current-density hydrogen evolution, Nat. Commun. 11 (2020) 3724.

[7] J. Li, J. Li, J. Ren, H. Hong, D. Liu, L. Liu, D. Wang, Electric-field-treated Ni/Co_3O_4 film as high-performance bifunctional electrocatalysts for efficient overall water splitting, Nano Micro Lett. 14 (2022) 148.

[8] L. Huang, R. Yao, X. Wang, S. Sun, X. Zhu, X. Liu, M.G. Kim, J. Lian, F. Liu, Y. Li, H. Zong, S. Han, X. Ding, *In situ* phosphating of Zn-doped bimetallic skeletons as a versatile electrocatalyst for water splitting, Energy Environ. Sci. 15 (2022) 2425–2434.

[9] G. Huang, Y. Li, R. Chen, Z. Xiao, S. Du, Y. Huang, C. Xie, C. Dong, H. Yi, S. Wang, Electrochemically formed PtFeNi alloy nanoparticles on defective NiFe LDHs with charge transfer for efficient water splitting, Chin. J. Catal. 43 (2022) 1101–1110.

[10] Y. Wang, X. Li, M. Zhang, J. Zhang, Z. Chen, X. Zheng, Z. Tian, N. Zhao, X. Han, K. Zaghib, Y. Wang, Y. Deng, W. Hu, Highly active and durable single-atom tungsten-doped $NiS_{0.5}Se_{0.5}$ nanosheet @ $NiS_{0.5}Se_{0.5}$ nanorod heterostructures for water splitting, Adv. Mater. 34 (2022) 2107053.

[11] T.I. Singh, A. Maibam, D.C. Cha, S. Yoo, R. Babarao, S.U. Lee, S. Lee, High-alkaline water-splitting activity of mesoporous 3D heterostructures: an amorphous-shell@ Crystalline-core nano-assembly of Co-Ni-phosphate ultrathin-nanosheets and V-doped cobalt-nitride nanowires, Adv. Sci. 9 (2022), 2201311.

[12] J. Sun, H. Xue, N. Guo, T. Song, Y.R. Hao, J. Sun, J. Zhang, Q. Wang, Synergetic metal defect and surface chemical reconstruction into $NiCo_2S_4$/ZnS heterojunction to achieve outstanding oxygen evolution performance, Angew. Chem. Int. Ed. 60 (2021) 19435–19441.

[13] B. Zhang, J. Shan, W. Wang, P. Tsiakaras, Y. Li, Oxygen vacancy and core–shell heterojunction engineering of anemone-like CoP@CoOOH bifunctional electrocatalyst for efficient overall water splitting, Small 18 (2022), 2106012.

[14] K. Li, J. Ma, X. Guan, H. He, M. Wang, G. Zhang, F. Zhang, X. Fan, W. Peng, Y. Li, 3D self-supported $Ni(PO_3)_2$–MoO_3 nanorods anchored on nickel foam for highly efficient overall water splitting, Nanoscale 10 (2018) 22173–22179.

[15] K. Chang, D.T. Tran, J. Wang, S. Prabhakaran, D.H. Kim, N.H. Kim, J.H. Lee, Atomic heterointerface engineering of Ni_2P-$NiSe_2$ nanosheets coupled ZnP-Based arrays for high-efficiency solar-assisted water splitting, Adv. Funct. Mater. 32 (2022), 2113224.

[16] Q. Yu, Z. Zhang, S. Qiu, Y. Luo, Z. Liu, F. Yang, H. Liu, S. Ge, X. Zou, B. Ding, W. Ren, H.M. Cheng, C. Sun, B. Liu, A Ta-TaS_2 monolith catalyst with robust and metallic interface for superior hydrogen evolution, Nat. Commun. 12 (2021) 6051.

[17] H. Liu, R. Xie, Y. Luo, Z. Cui, Q. Yu, Z. Gao, Z. Zhang, F. Yang, X. Kang, S. Ge, S. Li, X. Gao, G. Chai, L. Liu, B. Liu, Dual interfacial engineering of a chevrel phase electrode material for stable hydrogen evolution at 2500 mA cm^{-2}, Nat. Commun. 13 (2022) 6382.

[18] X. Zhang, J. Li, Y. Sun, Q. Liu, J. Guo, Hybridized $Ni(PO_3)_2$-$MnPO_4$ nanosheets array with excellent electrochemical performances for overall water splitting and supercapacitor, Electrochim. Acta 299 (2019) 835–843.

[19] X. Cheng, Z. Pan, C. Lei, Y. Jin, B. Yang, Z. Li, X. Zhang, L. Lei, C. Yuan, Y. Hou, A strongly coupled 3D ternary Fe_2O_3@Ni_2P/$Ni(PO_3)_2$ hybrid for enhanced electrocatalytic oxygen evolution at ultra-high current densities, J. Mater. Chem. A 7 (2019) 965–971.

[20] D.C. Liu, L.M. Cao, Z.M. Luo, D.C. Zhong, J.B. Tan, T.B. Lu, An *in situ* generated amorphous CoFePi and crystalline $Ni(PO_3)_2$ heterojunction as an efficient electrocatalyst for oxygen evolution, J. Mater. Chem. A 6 (2018) 24920–24927.

[21] A.G. Ramu, M.L.A. Kumari, M.S. Elshikh, H.H. Alkhamis, A.F. Alrefaei, D. Choi, A facile and green synthesis of CuO/NiO nanoparticles and their removal activity of toxic nitro compounds in aqueous medium, Chemosphere 271 (2021), 129475.

[22] Y. Li, Y. Wu, M. Yuan, H. Hao, Z. Lv, L. Xu, B. Wei, Operando spectroscopies unveil interfacial FeOOH induced highly reactive β-Ni(Fe)OOH for efficient oxygen evolution, Appl. Catal. B Environ. 318 (2022), 121825.

[23] C. Jin, P. Zhai, Y. Wei, Q. Chen, X. Wang, W. Yang, J. Xiao, Q. He, Q. Liu, Y. Gong, $Ni(OH)_2$ templated synthesis of ultrathin Ni_3S_2 nanosheets as bifunctional electrocatalyst for overall water splitting, Small 17 (2021), 2102097.

[24] L. Yang, Z. Guo, J. Huang, Y. Xi, R. Gao, G. Su, W. Wang, L. Cao, B. Dong, Vertical growth of 2D amorphous $FePO_4$ nanosheet on Ni foam: outer and inner structural design for superior water splitting, Adv. Mater. 29 (2017), 1704574.

[25] Q. Liu, C. Chen, J. Zheng, L. Wang, Z. Yang, W. Yang, 3D hierarchical $Ni(PO_3)_2$ nanosheet arrays with superior electrochemical capacitance behavior, J. Mater. Chem. A 5 (2017) 1421–1427.

[26] T. Zhou, H. Shan, H. Yu, C.A. Zhong, J. Ge, N. Zhang, W. Chu, W. Yan, Q. Xu, H. A. Wu, C. Wu, Y. Xie, Nanopore confinement of electrocatalysts optimizing triple transport for an ultrahigh-power-density zinc–air fuel cell with robust stability, Adv. Mater. 32 (2020), 2003251.

[27] Y. Hu, M. Guo, C. Hu, J. Dong, P. Yan, T. Taylor Isimjan, X. Yang, Engineering cobalt nitride nanosheet arrays with rich nitrogen defects as a bifunctional robust oxygen electrocatalyst in rechargeable Zn–air batteries, J. Colloid Interface Sci. 608 (2022) 2066–2074.

[28] C. Bai, S. Fan, X. Li, Z. Niu, J. Wang, Z. Liu, D. Zhang, Hollow Cu_2O@$CoMn_2O_4$ nanoreactors for electrochemical NO reduction to NH_3: elucidating the Void-confinement effects on intermediates, Adv. Funct. Mater. 32 (2022), 2205569.

[29] G. Cui, Y. Zeng, J. Wu, Y. Guo, X. Gu, X.W. Lou, Synthesis of nitrogen-doped KMn_8O_{16} with Oxygen vacancy for stable zinc-ion batteries, Adv. Sci. 9 (2022), 2106067.

[30] T. Jiang, W. Xie, S. Geng, R. Li, S. Song, Y. Wang, Constructing oxygen vacancy-regulated cobalt molybdate nanoflakes for efficient oxygen evolution reaction catalysis, Chin, J. Catal. 43 (2022) 2434–2442.

[31] Y. Chen, J. Wang, Z. Yu, Y. Hou, R. Jiang, M. Wang, J. Huang, J. Chen, Y. Zhang, H. Zhu, Functional group scission-induced lattice strain in chiral macromolecular metal-organic framework arrays for electrocatalytic overall water splitting, Appl. Catal. B Environ. 307 (2022), 121151.

[32] Y. Yin, J. Han, Y. Zhang, X. Zhang, P. Xu, Q. Yuan, L. Samad, X. Wang, Y. Wang, Z. Zhang, P. Zhang, X. Cao, B. Song, S. Jin, Contributions of phase, sulfur vacancies, and edges to the hydrogen evolution reaction catalytic activity of porous molybdenum disulfide nanosheets, J. Am. Chem. Soc. 138 (2016) 7965–7972.

[33] B. Wang, H. Huang, M. Huang, P. Yan, T.T. Isimjan, X. Yang, Electron-transfer enhanced MoO_2-Ni heterostructures as a highly efficient pH-universal catalyst for hydrogen evolution, Sci. China Chem. 63 (2020) 841–849.

[34] B. Wang, H. Huang, T. Sun, P. Yan, T.T. Isimjan, J. Tian, X. Yang, Dissolution reconstruction of electron-transfer enhanced hierarchical NiS_x-MoO_2 nanosponges as a promising industrialized hydrogen evolution catalyst beyond Pt/C, J. Colloid Interface Sci. 567 (2020) 339–346.

[35] Z. Niu, C. Qiu, J. Jiang, L. Ai, Hierarchical CoP–FeP branched heterostructures for highly efficient electrocatalytic water splitting, ACS Sustain. Chem. Eng. 7 (2019) 2335–2342.

[36] J. Yu, T. Zhang, Y. Sun, X. Li, X. Li, B. Wu, D. Men, Y. Li, Hollow FeP/Fe_3O_4 hybrid nanoparticles on carbon nanotubes as efficient electrocatalysts for the oxygen evolution reaction, ACS Appl. Mater. Interfaces 12 (2020) 12783–12792.

[37] R. Luo, Y. Li, L. Xing, N. Wang, R. Zhong, Z. Qian, C. Du, G. Yin, Y. Wang, L. Du, A dynamic $Ni(OH)_2$-NiOOH/NiFeP heterojunction enabling high-performance E-upgrading of hydroxymethylfurfural, Appl. Catal. B Environ. 311 (2022), 121357.

[38] A. Li, L. Zhang, F. Wang, L. Zhang, L. Li, H. Chen, Z. Wei, Rational design of porous Ni-Co-Fe ternary metal phosphides nanobricks as bifunctional electrocatalysts for efficient overall water splitting, Appl. Catal. B Environ. 310 (2022), 121353.

[39] X. Chen, Q. Wang, Y. Cheng, H. Xing, J. Li, X. Zhu, L. Ma, Y. Li, D. Liu, S-Doping triggers redox reactivities of both iron and lattice oxygen in FeOOH for low-cost and high-performance water oxidation, Adv. Funct. Mater. 32 (2022), 2112674.

[40] H. Li, C. Zhang, W. Xiang, M.A. Amin, J. Na, S. Wang, J. Yu, Y. Yamauchi, Efficient electrocatalysis for oxygen evolution: W-doped NiFe nanosheets with oxygen vacancies constructed by facile electrodeposition and corrosion, Chem. Eng. J. 452 (2023), 139104.

[41] X. Ding, J. Yu, W. Huang, D. Chen, W. Lin, Z. Xie, Modulation of the interfacial charge density on Fe_2P-CoP by coupling CeO_2 for accelerating alkaline electrocatalytic hydrogen evolution reaction and overall water splitting, Chem. Eng. J. 451 (2022), 138550.

[42] D.R. Paudel, U.N. Pan, R.B. Ghising, P.P. Dhakal, V.A. Dinh, H. Wang, N.H. Kim, J. H. Lee, Interface modulation induced by the 1T Co-WS_2 shell nanosheet layer at the metallic $NiTe_2$/Ni core–nanoskeleton: glib electrode-kinetics for HER, OER, and ORR, Nano Energy 102 (2022), 107712.

[43] B. Wang, K. Zhao, Z. Yu, C. Sun, Z. Wang, N. Feng, L. Mai, Y. Wang, Y. Xia, *In-situ* structural evolution of multi-site alloy electrocatalyst to manipulate intermediate for enhanced water oxidation reaction, Energy Environ. Sci. 13 (2020) 2200–2208.

[44] M. Chen, H. Li, C. Wu, Y. Liang, J. Qi, J. Li, E. Shangguan, W. Zhang, R. Cao, Interfacial engineering of heterostructured $Co(OH)_2$/NiP_x nanosheets for enhanced oxygen evolution reaction, Adv. Funct. Mater. 32 (2022), 2206407.

[45] M. Yu, J. Zheng, M. Guo, La-doped NiFe-LDH coupled with hierarchical vertically aligned MXene frameworks for efficient overall water splitting, J. Energy Chem. 70 (2022) 472–479.

[46] Y. Wang, Y. Du, Z. Fu, J. Ren, Y. Fu, L. Wang, Construction of Ru/FeCoP heterointerface to drive dual active site mechanism for efficient overall water splitting, J. Mater. Chem. A 10 (2022) 16071–16079.

[47] X. Mu, X. Gu, R. Zhou, L. Li, G. Lu, C. Chen, S. Liu, S. Mu, W. Chen, Metastable five-fold twinned Ru incorporated Cu nanosheets with Pt-like hydrogen evolution kinetics, Chem. Eng. J. 428 (2022), 131099.

[48] J.F. de Araújo, F. Dionigi, T. Merzdorf, H.S. Oh, P. Strasser, Evidence of mars-van-krevelen mechanism in the electrochemical oxygen evolution on ni-based catalysts, Angew. Chem. Int. Ed. 60 (2021) 14981–14988.

[49] T. Ai, H. Wang, W. Bao, L. Feng, X. Zou, X. Wei, L. Ding, Z. Deng, B. Rao, Fe-V synergistic doping effect of hierarchical Ni_3S_2 oblate-nanorod arrays for efficient electrocatalytic oxygen evolution reaction, Chem. Eng. J. 450 (2022), 138358.

[50] M. Gao, P. Gao, T. Lei, C. Ouyang, X. Wu, A. Wu, Y. Du, FeP/Ni_2P nanosheet arrays as high-efficiency hydrogen evolution electrocatalysts, J. Mater. Chem. A 10 (2022) 15569–15579.